

FAINT X-RAY BINARIES AND THEIR OPTICAL COUNTERPARTS IN M31

N. VULIC¹★, S. C. GALLAGHER¹, AND P. BARMBY¹

Draft version April 21, 2022

ABSTRACT

X-ray binaries (XRBs) are probes of both star formation and stellar mass, but more importantly remain one of the only direct tracers of the compact object population. To investigate the XRB population in M31, we utilized all 121 publicly available observations of M31 totalling over 1 Ms from *Chandra's* ACIS instrument. We studied 83 star clusters in the bulge using the year 1 star cluster catalogue from the Panchromatic Hubble Andromeda Treasury Survey. We found 15 unique star clusters that matched to 17 X-ray point sources within 1'' (3.8 pc). This population is composed predominantly of globular cluster low-mass XRBs, with one previously unidentified star cluster X-ray source. Star clusters that were brighter and more compact preferentially hosted an X-ray source. Specifically, logistic regression showed that the F475W magnitude was the most important predictor followed by the effective radius, while color (F475W–F814W) was not statistically significant. We also completed a matching analysis of 1566 H II regions and found 10 unique matches to 9 X-ray point sources within 3'' (11 pc). The H II regions hosting X-ray point sources were on average more compact than unmatched H II regions, but logistic regression concluded that neither the radius nor H α luminosity was a significant predictor. Four matches have no previous classification and thus are high-mass XRB candidates. A stacking analysis of both star clusters and H II regions resulted in non-detections, giving typical upper limits of $\approx 10^{32}$ erg s⁻¹, which probes the quiescent XRB regime.

Keywords: galaxies: individual: M31, NGC 224 — galaxies: H II regions — star clusters — X-rays: binaries — X-rays: galaxies

1. INTRODUCTION

Compact objects are the end-states of the evolution of massive stars and as such are signposts of the star formation history of a galaxy. X-ray binaries (XRBs) consist of a compact object, either a neutron star or black hole, which accretes matter from a companion star. Active XRBs have luminosities of $\sim 10^{35-41}$ erg s⁻¹ (those $> 10^{39}$ erg s⁻¹ are classified as ultra-luminous X-ray sources) while those in quiescence are $\lesssim 10^{34}$ erg s⁻¹. XRBs are classified into two main categories based on the mass of the companion star: low-mass (LMXB) and high-mass (HMXB) (Fabbiano 2006). LMXBs accrete matter via Roche lobe overflow while HMXBs transfer mass predominantly by Bondi-Hoyle (wind) accretion (Bondi & Hoyle 1944; Iben et al. 1995). LMXB formation is more efficient in globular clusters (GCs) than in the field of a galaxy due to the higher stellar densities in GCs (Katz 1975; Clark 1975; Fabian et al. 1975; Pooley et al. 2003). In the Milky Way, LMXB formation is approximately two orders of magnitude more efficient in GCs (Katz 1975; Clark 1975). Conversely, HMXBs are associated with star-forming regions (OB associations, H II regions, and infrared-bright dusty regions) as opposed to star clusters (Ranalli et al. 2003; Grimm et al. 2003; Swartz et al. 2004; Persic & Rephaeli 2007; Shtykovskiy & Gilfanov 2007; Lehmer et al. 2010; Walton et al. 2011; Swartz et al. 2011; Mineo et al. 2012a). Due to their evolutionary timescales, LMXBs trace the stellar mass of a galaxy (Gilfanov 2004; Kim & Fabbiano 2004; Zhang et al. 2011) while HMXBs probe the star formation rate (Grimm et al. 2003; Mineo et al. 2012a) within the past ~ 100 Myr (Shtykovskiy & Gilfanov 2007).

The Milky Way's XRBs have been studied extensively in

the Galactic Center, star clusters, and the field (e.g. Grimm et al. 2002; Revnivtsev et al. 2008; Muno et al. 2009; Bodaghee et al. 2012; Lutovinov et al. 2013; Nebot Gómez-Morán et al. 2013). Faint X-ray sources (quiescent XRBs, cataclysmic variables, millisecond pulsars, etc.) in the Milky Way have been studied to 10^{30} erg s⁻¹ and lower (Heinke et al. 2003; Sazonov et al. 2006; Heinke et al. 2006) as a result of *Chandra's* subarcsecond resolution and optical counterpart identifications with the *Hubble Space Telescope (HST)*. Due to dust obscuration, we can only probe X-ray sources in the plane of the disk out to ≈ 8 kpc from the Solar System. This hinders our ability to obtain a complete sample of the Galaxy's XRB population. Fortunately, M31 provides a convenient nearby analogue that allows us to perform an analysis of the faint X-ray population in a large galaxy.

M31's XRB population has been studied numerous times over the past decades with various X-ray telescopes (*X-ray Multi-Mirror Mission (XMM-Newton)*, *Röntgensatellit (ROSAT)*, *Einstein*). However, only the spatial resolution of *Chandra* allows us to study low-luminosity X-ray sources by separating them from the diffuse emission in the disk and crowding in the bulge. The LMXBs in M31 have been extensively studied by various groups (Trudolyubov & Priedhorsky 2004; Voss & Gilfanov 2007a,b; Peacock et al. 2010b; Zhang et al. 2011; Barnard et al. 2012b,a, 2013) that report on X-ray luminosity functions, spatial distributions, variability, and spectral analysis. Peacock et al. (2010b) used *XMM-Newton* to study 80% of the 416 confirmed GCs in M31 (Peacock et al. 2010a). They found 41 GCs associated with X-ray sources along with an additional 4 GCs identified with *Chandra* and *ROSAT*, for a total of 11% of GCs with X-ray sources. M31's GCs with LMXBs were found to be brighter, redder (metal-rich), and more compact than GCs without LMXBs, in agreement with other extragalactic XRB studies (Sivakoff et al. 2007; Paolillo et al. 2011; Mineo et al. 2014). Voss

¹ Department of Physics & Astronomy, Western University, London, ON, N6A 3K7, Canada

★ nvulic@uwo.ca

& Gilfanov (2007b) predicted a large number of faint transient sources in the bulge of M31, similar to the numerous faint X-ray sources (accreting millisecond pulsars) found in the Galactic Center (Muno et al. 2009).

A recent study by Stiele et al. (2011) with *XMM-Newton* covered all of M31 for the first time and reported on the X-ray source population compared to all previous studies. The survey catalogued 1897 point sources (914 new) and reached a limit of $\sim 10^{35}$ erg s $^{-1}$ in the 0.2 – 4.5 keV energy band. Sources were classified/identified by X-ray hardness ratios, spatial extent and distribution, cross-correlations in other wavelengths, and variability (using *Chandra* and *ROSAT* observations). They found 10 field LMXBs and 26 field LMXB candidates by analyzing long-term X-ray source variability. In addition, another 36 LMXBs were associated with GCs and 17 LMXB candidates were associated with GC candidates. No HMXBs were identified - in fact none have been confirmed in M31 to date - although 2 new candidates were proposed in addition to the 18 candidates from Shaw Greening et al. (2009). The comprehensive X-ray population analysis by Stiele et al. (2011) has classified hundreds of sources and shed light on their long-term variability and spatial/flux distributions. However, they pointed out that $\sim 65\%$ of their point sources are classified as “hard”, meaning that they have no optical identification and their X-ray colors are ambiguous: they could be XRBs, supernova remnants, or background active galaxies.

Barnard et al. (2014) have attempted to address the issue of unclassified X-ray point sources by identifying them using X-ray data alone. They used structure functions, which estimate the mean intensity deviation of data over a time interval. By determining structure functions for each source they constrained its variability and were able to differentiate XRBs from active galactic nuclei. They found 220 X-ray sources above $\geq 10^{35}$ erg s $^{-1}$ with significantly more variability than expected in the structure function for active galactic nuclei. Based on their analysis they classified these sources as XRBs, with an additional 30 XRB sources for a total of 250 probable XRBs (200 new) out of their sample of 528 X-ray sources in the central 20' of M31. Low-luminosity XRBs are more variable than luminous XRBs and thus are well-suited to this classification technique given sufficient signal-to-noise data.

One of the most powerful methods to confidently classify an X-ray source is identifying an optical counterpart. However, in crowded and extragalactic fields this generally requires the exquisite spatial resolution of *HST*. The ability to observe a large fraction of identified X-ray sources is limited since *HST* has both high demand and a small field of view. The Panchromatic *Hubble* Andromeda Treasury (PHAT) survey (Dalcanton et al. 2012) is a multicycle *HST* program to map one-third of M31's disk and provide an unprecedented catalogue of star clusters and stars. While it does not cover all of M31, it provides the best possible resource for determining optical counterparts to X-ray sources on such a large scale. M31's bulge has been monitored extensively with *Chandra*, whose 0.5'' point spread function (PSF) is superior to the 6'' provided by *XMM-Newton*.

To probe low-luminosity X-ray sources in M31 below the level achieved by Stiele et al. (2011), we will use the stacking method developed by Brandt et al. (2001b,c) and Hornschemeier et al. (2001). By stacking star cluster positions obtained from the PHAT survey and H II region positions (see Section 2.2) in a *Chandra* X-ray image of M31, we can de-

termine, on average, if these objects host faint point sources. Young star clusters and H II regions will probe the HMXB population while GCs will probe the LMXBs. Our study is not focused on the field population of XRBs. Stacking analyses enable us to study the effect that metallicity has on faint X-ray sources by separating metal-rich and metal-poor classes of GCs. Stacking is a unique way to investigate whether HMXBs in M31 exist but are below our current detection limits. By pushing extragalactic XRB luminosities into the quiescent regime ($< 10^{34}$ erg s $^{-1}$), we can reveal undetected populations that will help constrain binary evolution models (e.g. Hurley et al. 2002; Kiel & Hurley 2006; Belczynski et al. 2008; Lipunov et al. 2009; Bhadkamkar & Ghosh 2012, 2013; Siess et al. 2013; Bhadkamkar & Ghosh 2014).

We adopt a distance to M31 of 776 ± 18 kpc as in Johnson et al. (2012, hereafter J12), which corresponds to a linear scale of 3.8 pc arcsecond $^{-1}$. In Section 2, we describe the optical and X-ray observations and reduction procedure for the X-ray data. In Section 3, we report results from matching star clusters and H II regions to X-ray point sources. In Section 4, we present results from an X-ray stacking analysis of star clusters and H II regions. In Sections 5 and 6 we discuss our results and summarize our main conclusions.

2. OBSERVATIONS

2.1. X-ray Data

Chandra has observed M31 numerous times, but the small field of view (compared to *XMM-Newton*) of *Chandra*'s Advanced CCD Imaging Spectrometer (ACIS) instrument (8' \times 8' for ACIS-S and 16' \times 16' for ACIS-I) combined with the proximity of M31 require many pointings to cover an appreciable area of the galaxy. We use all 121 publicly available ACIS-S and ACIS-I observations in M31 for our matching and stacking analyses of star clusters and H II regions, having a total exposure time over 1 Ms. Due to the degradation of the PSF at large off-axis angles, we only use data from the S3 chip from the ACIS-S observations. The observations are listed in Tables 1 and 2 and their fields of view shown in Figure 1.

2.1.1. Data Reduction

Each observation was reprocessed with the *Chandra* Interactive Analysis of Observations (*CIAO*) tools package version 4.5 (Fruscione et al. 2006) and the *Chandra* Calibration database (*CALDB*) version 4.5.5 (Graessle et al. 2006). We started with the level-1 events file and produced a bad pixel file that identified observation-specific bad pixels, hot pixels, bright bias pixels, and afterglow events using `acis_run_hotpix`. Since we are studying faint sources, we ran `acis_detect_afterglow` to eliminate cosmic ray afterglows with only a few events. The level-1 events file was updated and filtered using the standard (ASCA) grades (0, 2 – 4, 6), status bits (0), good time intervals, charge transfer inefficiency (CTI), time-dependent gain, and pulse height with `acis_process_events`. We used the energy-dependent subpixel event repositioning algorithm to improve astrometry and, where necessary, set the VFaint option in `acis_process_events`.

We then created merged event files for all 26 ACIS-S observations and all 95 ACIS-I observations with `reproject_obs` to obtain fully-reduced images in the soft, hard, and full-bands corresponding to energy ranges of 0.3 – 2 keV, 2 – 8 keV, and 0.3 – 8 keV respectively. We produced exposure-corrected images (in units of photons cm $^{-2}$ s $^{-1}$ pixel $^{-1}$) with the `flux_obs`

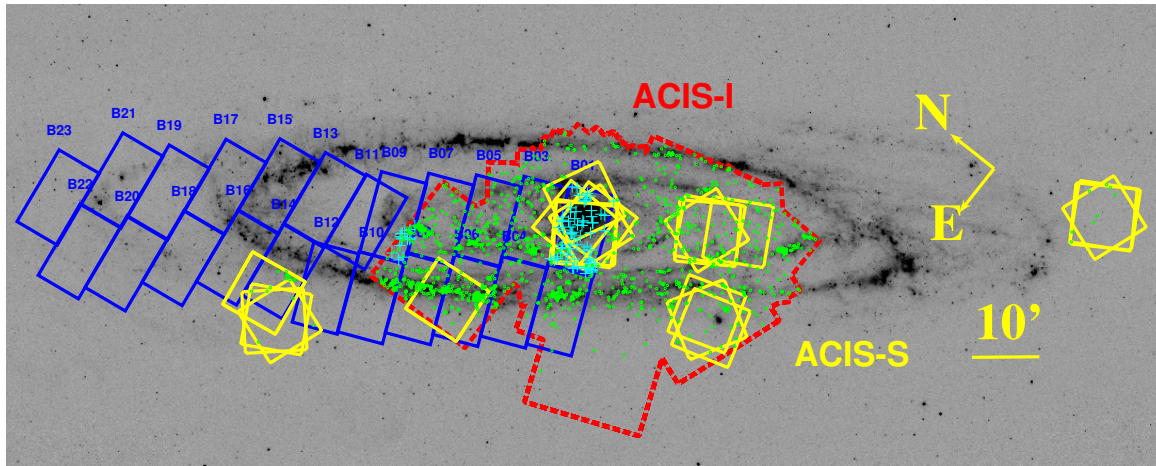


Figure 1. The field of view of the ACIS-I (dashed outline, red in the online version) merged observations and ACIS-S3 chips (yellow in the online version) for each observation used in our analysis overlaid on a Spitzer $24\ \mu\text{m}$ image of M31 (Gordon et al. 2006). The PHAT footprint is included with each rectangular brick (blue in the online version) labelled to show the overlap with *Chandra* data. The year 1 PHAT star cluster catalogue only includes bricks 1, 9, 15, 21, and parts of 17 and 23. Crosses (cyan in the online version) and circles (green in the online version) represent star clusters and H II regions, respectively, within the field of view of *Chandra* data (see Section 2.2 for more details). Most *Chandra* observations were part of an ongoing monitoring program of the supermassive black hole, while off-center ACIS-S pointings studied supersoft X-ray sources.

Table 1
ACIS-S Observations

ObsID ^a	Date	R.A. (J2000)	Decl. (J2000)	Livetime (s)	Datamode	CCDs	Roll Angle (degrees)
309	2000-06-01	10.688	41.27877	5129	FAINT	235678	87.5
310	2000-07-02	10.68311	41.27876	5284	FAINT	235678	108.7
313	2000-09-21	10.65816	40.87837	6002	FAINT	235678	162.9

Note. — Table 1 is published in its entirety in the electronic edition of the *Astrophysical Journal*. A portion is shown here for guidance regarding its form and content. Positions represent the aimpoint.

^a An asterisk indicates an interleaved observation.

Table 2
ACIS-I Observations

ObsID ^a	Date	R.A. (J2000)	Decl. (J2000)	Livetime (s)	Datamode	CCDs	Roll Angle (degrees)
303	1999-10-13	10.67806	41.26989	11890	FAINT	012367	193.0
305	1999-12-11	10.68273	41.26395	4185	FAINT	01236	274.0
306	1999-12-27	10.68409	41.2637	4189	FAINT	01236	285.4

Note. — Table 2 is published in its entirety in the electronic edition of the *Astrophysical Journal*. A portion is shown here for guidance regarding its form and content. Positions represent the aimpoint.

^a An asterisk indicates an interleaved observation.

tool using a bin size of 1 to maintain the native resolution. Weighted spectrum files (corresponding to the soft, hard, and full energy bands) were used to calculate instrument maps. The merged ACIS-S and ACIS-I images have dimensions² of $1.7^\circ \times 1.7^\circ$ and $0.8^\circ \times 0.85^\circ$ and correspond to exposures of ~ 548 ks and ~ 510 ks respectively³. The plate scale of the *Chandra* images is 0.5 arcsecond pixel^{-1} , corresponding to 1.9 pc pixel^{-1} . *Chandra*'s absolute astrometry is $\sim 0.6''$ at the 90% confidence level (Broos et al. 2010) and has spatial resolution that ranges from $1''$ on-axis to $4''$ at $4'$ off-axis for 1.5

keV at 90% encircled energy fraction for ACIS⁴.

2.1.2. X-Ray Point Source Detection

Given that we have produced deep images of M31's bulge, there may be new point sources that have not been previously identified. We used *wavdetect* on the full, hard, and soft-band images with scales⁵ of 1, 2, 4, 8, and 16 as recommended by the *Chandra* X-ray Center to have a wide range of source

² Since *Chandra* ACIS-S observations are sparse (Figure 1) large parts of the image are devoid of data.

³ These exposure times are not consistent across the fields of view since merging results in overlap of varying exposures from each observation.

⁴ <http://cxc.harvard.edu/proposer/POG/>

⁵ Using the $\sqrt{2}$ series from 1 to 8 we detected an additional 60 X-ray sources. However, this does not change the results of our matching analysis (see Section 3.1).

Table 3
X-ray Sources Detected in Merged ACIS Observations

Detector	Full	Hard	Soft	Total	Total Effective Sources
ACIS-I	435	344	388	1167	921
ACIS-S	353	217	334	904	

Note. — Total Effective Sources (ACIS-I & ACIS-S) refers to the number of actual X-ray sources detected after filtering those that appear in multiple energy bands and on both detectors. An internal match to within $0.5''$ filtered out sources with separations closer than the pixel scale.

sizes⁶. This ensures that the variation of the PSF at different off-axis angles is accounted for. Exposure maps were also input to reduce false positives. The sigthresh parameter, which determines how many false detections are allowed, should not be larger than the inverse of the number of pixels in the image being analyzed. Therefore it was set to 3×10^{-8} for the ACIS-I merged image and 7×10^{-9} for the ACIS-S merged image. These numbers are small since the ACIS-I merged image (0.68 deg^2) covers an area larger than the bulge and the ACIS-S merged image (2.89 deg^2) covers the majority of the galaxy even though only the nucleus and various pointings have data (see Figure 1 and Section 2.1.1). In any case, setting the sigthresh parameter to the default value of 10^{-6} did not change the number of X-ray sources matched to star clusters or H II regions. We obtained source lists for the full, hard, and soft-band merged ACIS-I and ACIS-S images. From the six source lists we collated our results into a master source list with the `match_xy` tool from the Tools for ACIS Review and Analysis (TARA) package⁷. We found a total of 1033 independent X-ray point sources across all 3 bands (a source was not necessarily detected in more than one band) for the ACIS-I merged observations and ACIS-S merged observations. We report the number of sources detected in each energy band for both ACIS-I and ACIS-S in Table 3. While the `match_xy` tool filtered X-ray sources based on their positional uncertainties from `wavdetect` (e.g. retains only one source position if detected in all 3 energy bands), `match_xy` does not consolidate pairs of extremely close `wavdetect` sources detected only in one band. We performed an internal match of our 1033 sources to remove sources within $0.5''$ of another source. This found a further 112 matches that we removed to obtain 921 effective X-ray sources.

We input our list of sources to the ACIS Extract package (Broos et al. 2010) along with exposure maps (calculated using weighted spectrum files) so that each observation could be individually analyzed. ACIS Extract then merged all observations (ACIS-I and ACIS-S) and produced the relevant source properties and statistics, such as X-ray luminosity. ACIS Extract aligns each observation to a published astrometric catalogue⁸ and thus gives precision of $\sim 0.1''$ for most point sources. We required ACIS Extract’s `PROB_NO_SOURCE` statistic for each X-ray source to be $> 99.9\%$, except where by-eye inspection of the images showed source crowding that biased this statistic to lower values (i.e. 5 sources included that were not $> 99.9\%$). The majority of our sources ($\sim 75\%$) are located in the bulge, where the *Chandra* observations

are deeper compared with the rest of the galaxy. We only processed (through ACIS Extract) the 26 X-ray sources that matched to star clusters and H II regions (see Section 3.1 for details). The luminosity range of these 26 X-ray sources was $8.5 \times 10^{33} \text{ erg s}^{-1}$ to $7.8 \times 10^{37} \text{ erg s}^{-1}$. There is no meaningful, single value for the completeness limit since the exposure time varies significantly across the usable field of view. The deepest exposure of any 1 pixel reaches $\sim 500 \text{ ks}$ in both the merged ACIS-I and merged ACIS-S images; this occurs in the nucleus and corresponds to a sensitivity limit of $\approx 10^{33} \text{ erg s}^{-1}$. The complete X-ray point source catalogue will follow in a subsequent paper (Vulic et al., in prep.).

2.2. Optical Data

We use the star cluster catalogue compiled by J12 from the PHAT survey. The survey operates using the Advanced Camera for Surveys (filters F475W and F814W) as well as the Wide Field Camera 3 (filters F275W, F336W, F110W, and F160W) on the *HST*. The observational technique used by the survey is detailed in Dalcanton et al. (2012) and comprises 23 areas known as “bricks”, with each one consisting of 18 different fields of view. The survey produces photometry with a signal-to-noise ratio of 4 at $m_{F275W} = 25.1$, $m_{F336W} = 24.9$, $m_{F475W} = 27.9$, $m_{F814W} = 27.1$, $m_{F110W} = 25.5$, and $m_{F160W} = 24.6$ for single pointings in the uncrowded outer disk. The PHAT year 1 star cluster catalogue was compiled from bricks 1, 9, 15, 21, and parts of 17 and 23. Due to the limited *Chandra* data we only utilize brick 1 and a small part of brick 9 (proposal 12058, PI: Julianne Dalcanton). Even though Figure 1 shows numerous PHAT bricks coincident with *Chandra* data, the only bricks with published star cluster catalogues that overlap are 1 and 9. There are 83 star clusters⁹ in the field of view of the *Chandra* observations that we use for our matching and stacking analyses (indicated by crosses in Figure 1). J12 have corrected the absolute astrometry to agree with the 2MASS reference system within $\sim 60 \text{ mas}$. The PSF (full width at half maximum) for F475W is $\approx 0.10'' - 0.13''$ (Ubeda & et al. 2012).

In addition, we use the new catalogue of H II regions in M31 compiled by Azimlu et al. (2011). M31’s entire disk is covered out to $\sim 24 \text{ kpc}$ from the center based on observations with the Mayall 4 m telescope as part of the Nearby Galaxies Survey (Massey et al. 2006). A total of 3691 H II regions down to $L_{H\alpha} = 10^{34} \text{ erg s}^{-1}$ are identified in the 2.2 deg^2 mosaic, with 1566 in the field of view of the *Chandra* data (indicated by circles in Figure 1). The average PSF (full width at half maximum) of the survey was $1''$, which is generally better than *Chandra*’s range of $1'' - 4''$ but not as good as the $\approx 0.10'' - 0.13''$ for F475W from the PHAT survey. The astrometric calibration of the H II region catalogue is good to $0.1''$, better than *Chandra*’s $0.6''$ but not as precise as the 60 mas for PHAT.

3. DATA ANALYSIS

3.1. Matching Results

Prior to stacking star clusters and H II regions we must exclude those with identified X-ray point sources. Stacking probes faint X-ray point sources by co-adding star clusters (or H II regions) that are undetected in X-rays. In this way one hopes to detect a signal in the source aperture (centered on the position of the star cluster or H II region) above the

⁶ <http://cxc.harvard.edu/ciao/ahelp/wavdetect.html#plist.scales>

⁷ <http://www2.astro.psu.edu/xray/docs/TARA/>

⁸ Naval Observatory Merged Astrometric Dataset (Zacharias et al. 2004) or 2MASS Point Source Catalog (Skrutskie et al. 2006)

⁹ A PHAT year 1 ‘possible cluster’ catalogue exists that we have not used.

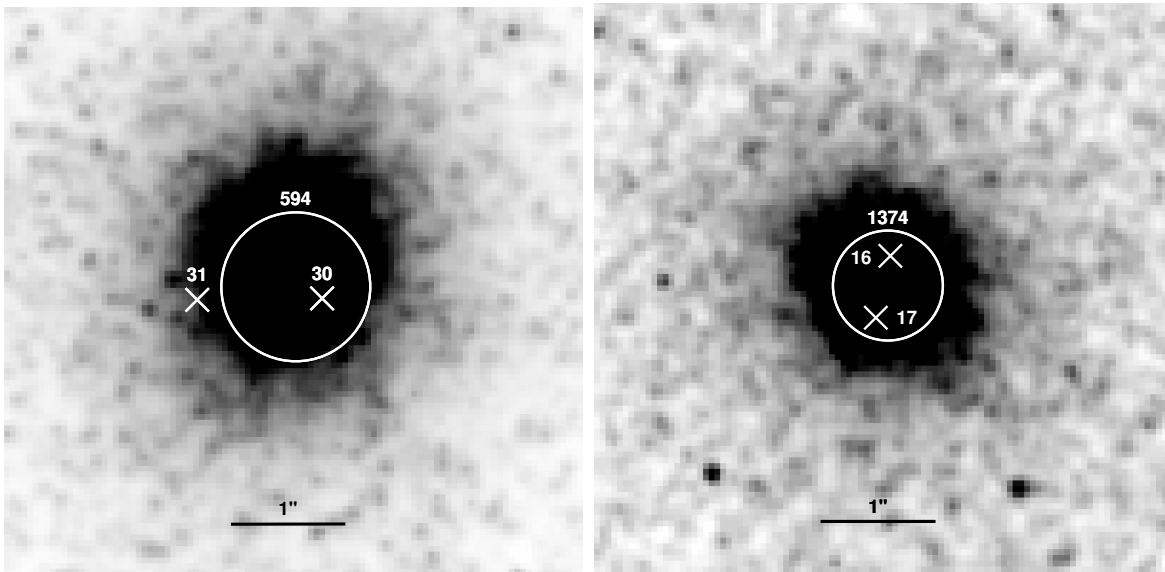


Figure 2. Images from the F475W band of the PHAT survey showing star clusters with double X-ray point source matches, where each panel is $5''$ on a side. White circles represent star clusters (with the radius equal to the effective radius of the star cluster) while an “X” represents the position of an X-ray source. The numbers correspond to the PHAT and AE identification numbers respectively from Table 4.

background (see Section 4 for more details). Therefore, including a star cluster (or H II region) with a detected X-ray point source in the complete stack of all undetected star clusters (or H II regions) would defeat the purpose of detecting a faint X-ray source in the stack. Figure 1 shows where the star clusters and H II regions we analyzed are located in M31. The 83 star clusters in the field of view of *Chandra* data are located mainly in the bulge (PHAT brick 1), while a handful are in the disk (PHAT brick 9); the 1566 H II regions are spread throughout the disk. Here we summarize our matching results, beginning with star clusters.

We used TOPCAT (Taylor 2005) to complete a matching analysis with the 83 star clusters and 921 X-ray point sources. A total of 15 star clusters were matched to 17 unique X-ray point sources within $1''$. The matching results are shown in Table 4. Two star clusters (PHAT IDs 594 and 1374) each had two X-ray point source matches. Figure 2 shows these star clusters in the F475W band image from PHAT. The clusters are plausible double XRB hosts since the X-ray sources are separated by $>0.5''$. Even though we used a $1''$ matching radius, only 2 star clusters (PHAT IDs 1403 and 1415) had a separation $>0.5''$ from their matched X-ray point source. No additional clusters were matched when increasing the matching radius to $>10''$. Only one star cluster (PHAT ID 1374) has not previously been associated with an X-ray source. In addition, one star cluster (PHAT ID 1375) that was previously identified as a GC candidate X-ray source by (Voss & Gilfanov 2007a) was not associated with an X-ray source in our analysis. Upon further inspection of our ACIS-I image it seemed that wavdetect did not identify what was likely an X-ray source.

To address the chance coincidence probability of our matches we created 25 source lists from our original X-ray catalogue that offset each source by $\pm 5-10''$ (Antoniou et al. 2009; Zezas et al. 2002). A false-match rate of $\sim 2\%$ was recovered (≤ 1 false match). We also used the cumulative number counts of Brandt et al. (2001a) to estimate the expected background sources in the 83 star cluster regions of radius $1''$ each. In equation 1, S is the flux in erg s^{-1}

cm^{-2} and N is the number of background sources per deg^2 above that flux, where we used the faintest X-ray point source from our matches ($\approx 1.4 \times 10^{-16} \text{ erg s}^{-1} \text{ cm}^{-2}$). This gave $N(> 1.4 \times 10^{-16} \text{ erg s}^{-1} \text{ cm}^{-2}) = (9.4 \times 10^{-4})^{+5.4 \times 10^{-4}}_{-1.3 \times 10^{-3}}$ expected background sources, indicating that our matches are likely authentic. We also completed cone searches in the NASA/IPAC Extragalactic Database (NED) within $30''$ around each of the 17 X-ray point sources that were matched to star clusters and found no background galaxies.

$$N(> S) = 3970 \left(\frac{S}{1 \times 10^{-16}} \right)^{-0.67 \pm 0.14} \text{ deg}^{-2} \quad (1)$$

Our results show that $\sim 18\%$ (15/83) of star clusters were matched to an X-ray point source within $1''$. In a survey of eight Fornax and Virgo elliptical galaxies (limiting luminosities typically few $\times 10^{37} \text{ erg s}^{-1}$) Kim et al. (2013) found that 408 of 5904 ($\sim 7\%$) GCs are associated with an X-ray source within $0.5''$. Similarly, a survey of 11 Virgo Cluster early-type galaxies (limiting luminosities typically few $\times 10^{37} \text{ erg s}^{-1}$) by Sivakoff et al. (2007) found that 270 of 6488 ($\sim 4\%$) GCs were associated with an X-ray source within $1''$. Our analysis was restricted to the bulge/central region of M31 and thus the concentration of X-ray point sources is larger than throughout the rest of the galaxy (as Munro et al. 2009 found for the Milky Way). Since LMXBs trace stellar mass (Gilfanov 2004), and stellar mass density is larger in the bulge, we would therefore expect to have a higher percentage of matches (LMXBs) compared to the value for the entire galaxy. Additionally, our luminosity limit is a factor of 10^3 fainter than previous surveys and therefore increases our percentage of matches. To more directly compare different galaxies, we compare the fraction (and number) of GCs with an LMXB versus those without above a given luminosity limit from our survey with those of Sivakoff et al. (2007) and Kim et al. (2013) in Table 5. We compared our results to individual galaxies from these two surveys since most galaxies they studied had varying limiting L_X (i.e. their complete sample is not completeness-corrected). The fractions are comparable (e.g. 6% for our work and 6.5%

Table 4
Star Cluster & X-ray Point Source Matches

Star Cluster Positions ^a			Results from ACIS Extract								Group Data ^b			Previous Classification	
PHAT ID	RA (J2000)	Dec	AE ID	RA (J2000)	Dec	PErr ^c (")	Prob ^d	OAA ^e (°)	PSF %	$\log(L_X)^f$ (erg s^{-1})	ID	Size	Sep (")	Class ^g	Ref. ^h
594	10.856666	41.260284	30	10.856581	41.260256	0.00	1.00 ⁱ	4.3	0.4	33.32	1	2	0.25	GC	HO
594	10.856666	41.260284	31	10.856984	41.260252	0.00	1.00 ⁱ	4.3	0.4	33.37	1	2	0.87	GC	HO
1374	10.711676	41.285381	16	10.711668	41.285453	0.15	0.11 ^j	1.6	0.39	34.24	2	2	0.26
1374	10.711676	41.285381	17	10.711715	41.285303	0.25	0.70 ^j	1.6	0.39	27.88 ^k	2	2	0.30
612	10.749429	41.268238	21	10.749429	41.268268	0.01	0.00	3.5	0.9	37.61	0.11	GC/BH?	ZH/BA
616	10.766111	41.301309	24	10.766068	41.301343	0.01	0.00	2.0	0.39	37.42	0.17	GC/BH?	ZH/BA
642	10.794234	41.247575	27	10.794231	41.2476	0.02	0.00	3.1	0.39	37.82	0.09	GC/BH?	ZH/BA
663	10.762226	41.25627	23	10.7622	41.256281	0.01	0.00	3.2	0.4	37.37	0.08	GC/BH?	VO/BA
682	10.814255	41.190284	28	10.814253	41.190228	0.13	0.00	7.0	0.9	35.98	0.20	GC	VO
1377	10.731713	41.309748	19	10.731691	41.309742	0.02	0.00	3.1	0.39	36.39	0.06	fgStar/GC	VO/KO
1381	10.692025	41.293409	13	10.692013	41.293426	0.03	0.00	1.5	0.39	35.91	0.07	GC	KO
1386	10.63027	41.327441	6	10.630254	41.327479	0.01	0.00	4.2	0.4	37.24	0.14	GC	VO
1395	10.672678	41.256623	10	10.672652	41.256609	0.01	0.00	1.0	0.39	36.51	0.09	GC	VO
1401	10.638559	41.295108	7	10.638544	41.295104	0.02	0.00	2.6	0.9	36.31	0.04	GC	HO
1403	10.623894	41.2993	4	10.624093	41.299152	0.39	0.00	3.5	0.9	34.79	0.76	GC	ZH
1415	10.68207	41.211915	11	10.681932	41.211796	0.28	0.07	3.7	0.9	33.82	0.57	GC	HO
1444	10.58984	41.238797	3	10.589851	41.238801	0.20	0.00	4.2	0.4	35.85	0.03	IRsrc	KA

^a Taken from the catalogue of J12.

^b Group ID identifies star clusters that were matched to multiple X-ray point sources (Group Size).

^c Source positional uncertainty.

^d Probability source does not exist.

^e Average off-axis angle.

^f In the 0.3 – 8 keV band.

^g BH = Black Hole, GC = globular cluster, fgStar = foreground star, IRsrc = infrared source, ? indicates a candidate.

^h BA (Barnard et al. 2013), HO (Hofmann et al. 2013), KA (Kaaret 2002), KO (Kong et al. 2002), VO (Voss & Gilfanov 2007a), ZH (Zhang et al. 2011).

ⁱ X-ray sources located at the edge of ACIS-S image and thus only contribute to the background, resulting in a large probability.

^j Suffer from crowding and thus have unreasonably high values.

^k Source has a large A_V from best-fit XSPEC (Arnaud 1996) model and thus the luminosity is unreliable.

for Sivakoff et al. 2007) at low- L_X limits ($L_X > 5 \times 10^{37}$ erg s^{-1}). For $L_X > 2.6 \times 10^{37}$ erg s^{-1} a fraction of 3.6% found in our study is much lower than the 8.3% of Kim et al. (2013). In general, we and Sivakoff et al. (2007) find a difference in the fraction that is lower by a factor of 2 – 4 than Kim et al. (2013) for $L_X > 2.6 \times 10^{37}$ erg s^{-1} , which could be attributed to small-number statistics. When analyzing the same galaxies as Sivakoff et al. (2007), Kim et al. (2013) found more GC-LMXBs as a result of deeper X-ray observations over an extended period of time, which also allowed for the identification of previously quiescent sources that went into outburst.

Of the 1566 H II regions in the field of view, we found 10 that matched to 9 unique X-ray point sources within 3'' (~11.2 pc, their average radius). The results are shown in Table 6. The false-match rate for H II regions was ~35%, which is higher due to the increased matching radius and their larger physical size compared to star clusters. For each of the 9 X-ray point sources that were matched to H II regions, we completed NED cone searches using a radius of 30''. Only one source (AE ID 38, 2.3'' from an H II region; see Table 6) had any nearby entries in NED. These were a nova at a distance of 0.4'', an H II region at a distance of 3.2'', and a background galaxy at a distance of 7''. We summarize our matching results and state completeness limits in Table 7.

3.2. X-ray Properties of Matched Star Clusters & H II Regions

An X-ray color-color plot of the X-ray point sources matched to star clusters and H II regions is shown in Figure 3, with the X-ray color classification scheme of Kilgard et al. (2005) overlaid. Soft and hard colors are defined by the soft

(S, 0.3 – 1 keV), medium (M, 1 – 2 keV), hard (H, 2 – 8 keV), and total (T, 0.3 – 8 keV) band energies as $(M - S)/T$ and $(H - M)/T$ respectively. X-ray photometry was completed separately for each observation for each X-ray point source. The photometry results for each observation were then merged for each X-ray point source in each of the energy bands to determine colors. Due to the variation in the spectral states of XRBs, the same source can end up in different areas of the diagram. Also, only flux measurements account for the changing effective area of *Chandra*, whereas counts do not. Since the observations we used were spread over 13 years, using counts introduces another source of uncertainty. Absorption also moves X-ray sources into different regions of the diagram and thus can result in misclassifications. Most of the sources are clustered between the XRB and background source regions. However, given the low false match rate for star clusters and previous confirmations as GC sources it is likely that these are mostly XRBs. The X-ray source with AE ID #3 has a luminosity typical of bright XRBs and was previously classified to match within 0.1'' of an infrared source by Kaaret (2002). The remaining X-ray sources were already identified as GCs by various studies (see Table 4 for refs.) with many that are likely black hole XRBs (Barnard et al. 2013).

3.3. Optical Properties of Matched Star Clusters and H II Regions

A color-color diagram of the 83 star clusters (J12) in the *Chandra* coverage region is shown in Figure 4. A theoretical evolutionary track from the simple stellar population models of Marigo et al. (2008) with $Z = 0.02$ is overlaid after apply-

Table 5
GC-LMXB Fraction Comparisons

Study	Galaxies	Percentage of GCs with an LMXB (10^{38} erg s $^{-1}$)				
		≥ 0.05	≥ 0.09	≥ 0.14	≥ 0.26	≥ 0.3
This work	M31	6% (5)	6% (5)	6% (5)	3.6% (3)	2.4% (2)
Kim et al. (2013) ^a	NGC 4365, NGC 4649	8.3% (209)	...
	NGC 4472	9.2% (70)
Sivakoff et al. (2007) ^b	NGC 4374, NGC 4697	6.5% (52)
	NGC 4365, NGC 4406	...	3.8% (49)
	NGC 4486, NGC 4552	3.8% (80)
	NGC 4526	2.9% (7)

Note. — Values shown in brackets represent the number of GC-LMXBs. Since the comparison studies do not publish values above a given L_X for the entire sample we can only compare individual galaxies.

^a Sample of Virgo and Fornax cluster early-type galaxies; uses $L_{X,min}$ (0.3–10 keV) as limiting luminosity.

^b Sample of Virgo cluster early-type galaxies; uses $L_{X,min}$ (0.3–8 keV) at 50% detection probability as limiting luminosity.

Table 6
H II Region & X-ray Point Source Matches

H II Region Data ^a						Results from ACIS Extract							Group Data ^b			Previous Classification	
H II ID	RA (J2000)	Dec	Radius (pc)	$\log(L_{H\alpha})$ (erg s $^{-1}$)	AE ID	RA (J2000)	Dec	PErr ^c (")	Prob ^d	OAA ^e ($^{\circ}$)	PSF %	$\log(L_X)^f$ (erg s $^{-1}$)	ID	Size	Sep (")	Class ^g	Ref. ^h
2165	10.8667	41.3092	10.99	36.87	33	10.866947	41.309129	0.14	0.00	7.8	0.5	35.94	1	2	0.7	SNR	WI/ST
2164	10.8667	41.3091	10.43	36.94	33	10.866947	41.309129	0.14	0.00	7.8	0.5	35.94	1	2	0.7	SNR	WI/ST
1686	10.6429	40.9527	13.33	35.31	8	10.643727	40.95233	0.46	0.00	4.2	0.9	35.87	2.6	GC	PE/ZH/ST
1798	10.7046	41.4017	7.83	36.72	14	10.704479	41.402351	0.28	0.00	7.9	0.9	35.53	2.4	SNR	ST
1805	10.7083	40.8914	8.62	34.44	15	10.707519	40.891337	0.59	0.00	3.7	0.9	34.86	2.1
1831	10.7233	41.4307	9.48	36.91	18	10.722953	41.430795	0.31	0.00	9.3	0.9	35.99	1.0	SNR	ST/VO
2080	10.8287	41.338	7.83	35.64	29	10.828635	41.338083	0.25	0.00	7.2	0.9	35.61	0.3	SSS?	HO/ST
2241	10.885	41.3499	7.83	35.11	34	10.884631	41.349752	1.09	0.23	8.6	0.9	35.02	1.1
2471	10.9721	41.2017	10.43	36.03	36	10.972348	41.200971	0.62	0.00	6.9	0.9	35.44	2.7
3005	11.1367	41.4225	7.83	37.52	38	11.13587	41.422606	0.76	0.00	3.9	0.9	35.11	2.3

^a Taken from the catalogue of Azimlu et al. (2011).

^b Group ID identifies an H II region matched to multiple X-ray point sources (Group Size).

^c Source positional uncertainty.

^d Probability source does not exist.

^e Average off-axis angle.

^f In the 0.3–8 keV band.

^g SNR = supernova remnant, GC = globular cluster, SSS = supersoft X-ray source, ? indicates a candidate.

^h WI (Williams et al. 2004), ST (Stiele et al. 2011), PE (Peacock et al. 2010b), ZH (Zhang et al. 2011), VO (Voss & Gilfanov 2007a), HO (Hofmann et al. 2013).

Table 7
Matching Analysis Summary

Type	Completeness Limit	Matched	Matched X-ray Sources
PHAT Star Clusters	$M_{F475W} = -4.0$ & $M_{F814W} = -5.0$	15	17
H II Regions	$L_{H\alpha} = 10^{34}$ erg s $^{-1}$	10	9

Note. — The H II region catalogue (Azimlu et al. 2011) reports a limiting luminosity but not a completeness limit; the star cluster catalogue (J12) is 80% complete to the indicated magnitudes. X-ray sources have a limiting luminosity of 8.5×10^{33} erg s $^{-1}$.

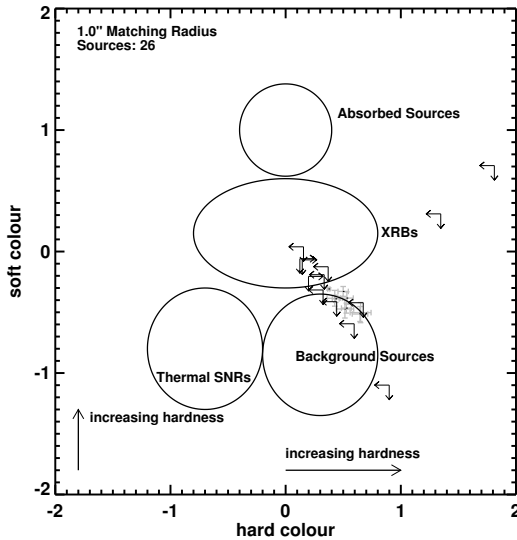


Figure 3. X-ray color-color diagram of the 26 X-ray point sources in M31 that were matched to star clusters or H II regions. The X-ray color classification scheme of Kilgard et al. (2005) is overlaid. Sources that were not detected in one or more energy bands ($< 3\sigma$) are plotted as upper or lower limits in one or both axes. Misclassification can result from the variation of XRBs spectral states over time. Also, since counts do not incorporate the change in effective area of *Chandra* over time, additional uncertainty is introduced because observations are spread over 13 years. Most sources are found in the region of color space between XRBs and background sources, where previous classifications from Table 4 confirm the majority of those matched to star clusters as GC-LMXBs.

ing a total reddening (external and internal) of $E(B-V) = 0.13$ (Caldwell et al. 2011). The 15 star clusters correspond to the 17 X-ray point sources they were matched to from Figure 3 (results in Table 4). In Figure 4 most star clusters are ≥ 1 Gyr old as expected for an old bulge population.

To determine whether our matches correspond to brighter and redder star clusters, we created the color-magnitude diagram shown in Figure 5. It is evident that the matches are all brighter and redder than star clusters without a detected X-ray point source. This is in agreement with the studies of GC-LMXBs in both elliptical and spiral galaxies mentioned earlier (Sivakoff et al. 2007; Peacock et al. 2010b; Paolillo et al. 2011; Mineo et al. 2014). The average F475W magnitude of matched star clusters was 17 ± 0.6 compared to 20.7 ± 0.6 for unmatched clusters, while the average effective radius of matched clusters was 1.6 ± 0.1 pc compared to 2 ± 0.1 pc for unmatched clusters¹⁰. This confirms the trend that more luminous, compact star clusters preferentially host an X-ray source. Further evidence is shown in the left panel of Figure 6, where it is clear that our matches are all above the 80% completeness limit ($m_{F475W} = 20.47$) mentioned in Table 7. Figure 7 shows the X-ray luminosity of point sources that were matched to star clusters plotted against the F475W magnitude and effective radius R_{eff} . The histograms show that our sample (dark portion) has preferentially more bright clusters than the complete year 1 sample (black outline - mostly disk clusters), while no significant variations in R_{eff} between the samples is seen. Specifically, the F475W magnitudes of our sample are skewed towards the bright end compared to the complete sample. We performed a Kolmogorov-Smirnov (KS) test on the two distributions, namely our sample and the complete year 1 sample of star clusters, for both the F475W

¹⁰ Uncertainties were not published for R_{eff} so we computed the standard error of the mean.

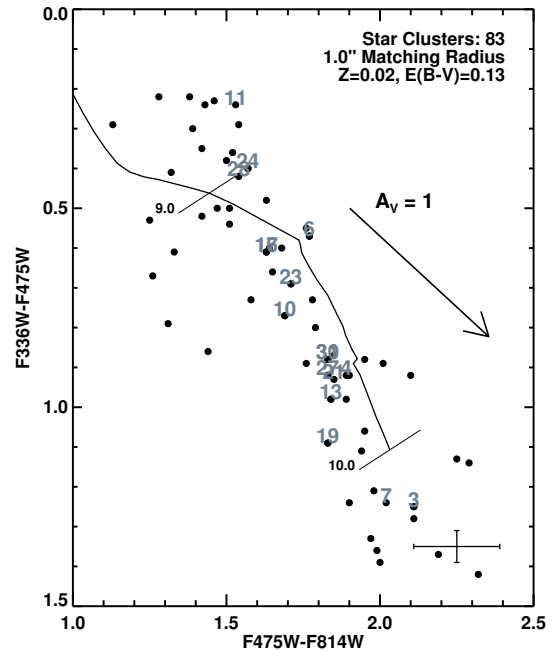


Figure 4. Optical color-color diagram of the 83 star clusters in M31 from the catalogue of J12 that are within the field of view of the *Chandra* X-ray image. A theoretical evolutionary track from the simple stellar population model of Marigo et al. (2008) with $Z = 0.02$ is included with a total reddening (external and internal) of $E(B-V) = 0.13$ applied (Caldwell et al. 2011). Bars on the track represent $\log(\text{age})$ in years. Numbers labelling individual data points indicate the AE IDs of the 17 unique X-ray point sources that matched to 15 star clusters (Table 4). The foreground reddening vector is of length $A_V = 1$ mag.

magnitude and R_{eff} . We found that the probability that the two distributions are drawn from the same sample is 3.7×10^{-14} for the F475W magnitude and 0.09 for R_{eff} , confirming that the F475W magnitudes of the two distributions are different.

To assess the statistical significance of our results we used the **R** statistical software (R Development Core Team 2008) to complete a logistic regression on our data. This allows us to assess the impact that a parameter has on the probability of a star cluster hosting an X-ray source. The generalized linear model (*glm*) in **R** is best-suited for this and has the form shown in equation 2, where p_i is the probability of success averaged over i trials (outcome of 1 or 0, i.e. matched or not) and the β_m 's are the regression coefficients of the variables $x_{m,i}$ that we model.

$$\ln\left(\frac{p_i}{1-p_i}\right) = \beta_0 + \beta_1 x_{1,i} + \dots + \beta_m x_{m,i} \quad (2)$$

For star clusters we modelled 3 variables, specifically the effective radius R_{eff} , F475W magnitude, and color (F475W-F814W). We only included the 83 star clusters that were in the field of view of the *Chandra* data, since only these star clusters could possibly have been matched to an identified X-ray point source. The results of the logistic regression are shown in Table 8.

Since a variable in the model is generally significant for a p -value $\Pr(> |z|) < 0.05$ (i.e. null hypothesis is rejected), only R_{eff} and the F475W magnitude are statistically significant. From Table 8 the coefficient gives the \ln odds increase of a match for a unit increase in the respective variable. Therefore, a unit increase in R_{eff} results in a decrease of ≈ 21 in the \ln odds. However, because each variable has a different

Table 8
Logistic Regression Results for Star Clusters and H II regions

Variable	Coefficient β	Standard Error	z -Value	$\text{Pr}(> z)$
Star Clusters				
R_{eff}	-20.7241	9.0953	-2.279	0.02269
F475W	-2.9285	1.0582	-2.767	0.00565
F475W - F814W	0.5696	2.2257	0.256	0.79802
H II regions				
Radius	-0.9283	2.7518	-0.337	0.736
H α Luminosity	13.9974	36.3963	0.385	0.701

Note. — Results for a model fit to equation 2. The z -statistic in column 4 tells us how many standard error units the sample mean is from the population mean while the p -value in the last column gives us the probability that the null hypothesis is true. A variable in the model is significant for a p -value $\text{Pr}(>|z|) < 0.05$.

range of values, a unit increase does not have a 1:1 correspondence across variables. Therefore the smallest p -value indicates which variable is most important to the outcome. From this we see that the F475W magnitude is more significant when determining if a star cluster hosts a bright X-ray source, followed by the effective radius. However, star cluster color was not important, at odds with the surveys of GC-LMXBs in spiral and elliptical galaxies mentioned above. These surveys studied entire galaxy populations, meaning that even if GC catalogues were incomplete their numbers were not radically biased towards metal-poor or metal-rich. Our result could be a consequence of our sample since it was restricted mostly to bulge clusters, which are metal-rich (see Figure 5). Indeed, a KS test between the F475W-F814W color of star clusters in our sample and the complete year 1 PHAT clusters gives a probability of 1.7×10^{-13} that the two distributions are drawn from the same sample. This confirms that bulge clusters are more metal-rich than those in the disk. Complete surveys of M31's GCs by Peacock et al. (2010b) and Agar & Barmby (2013) showed that metal-rich star clusters were more likely to host an X-ray source, indicating our result is biased by our sample.

The 10 H II regions matched to X-ray sources have average radii and H α luminosities of $R = 9.4 \pm 0.6$ pc and $L_{\text{H}\alpha} = 1.4 \pm 0.2 \times 10^{36}$ erg s $^{-1}$ compared to averages of $R = 11.2 \pm 0.2$ pc and $L_{\text{H}\alpha} = 1.2 \pm 3.2 \times 10^{36}$ erg s $^{-1}$ for unmatched H II regions¹¹. While H II regions that were matched to X-ray point sources seem to favour those that are more compact, we cannot claim a trend exists with H α luminosity due to the large errors associated with their average values. The right panel of Figure 6 shows the distribution of H II region luminosity and radius, with matches crowding the compact end. However, H II regions have a much wider range of radii than globular clusters and generally are not well approximated by circular apertures (Azimlu et al. 2011). These differences complicate comparisons between the populations. The limiting $L_{\text{H}\alpha}$ for H II regions from Table 7 applies across the entire R_{eff} range; those with larger radii naturally have a larger luminosity and are not biased by incompleteness.

As for star clusters we also completed logistic regression on the 1566 H II regions that were in the field of view of the *Chandra* data. We modelled the radius and H α luminosity of

H II regions to assess their impact on the probability of hosting an X-ray source, with the results shown in Table 8. From the p -values of both variables we can see that neither is significant in determining the presence of an X-ray source as both are $\gg 0.05$. In the right panel of Figure 6 it would seem that at least the most compact H II regions were more likely to host an X-ray source. However, based on the distribution of the population, specifically that most H II regions have small radii, this impression is not supported by our statistical analysis.

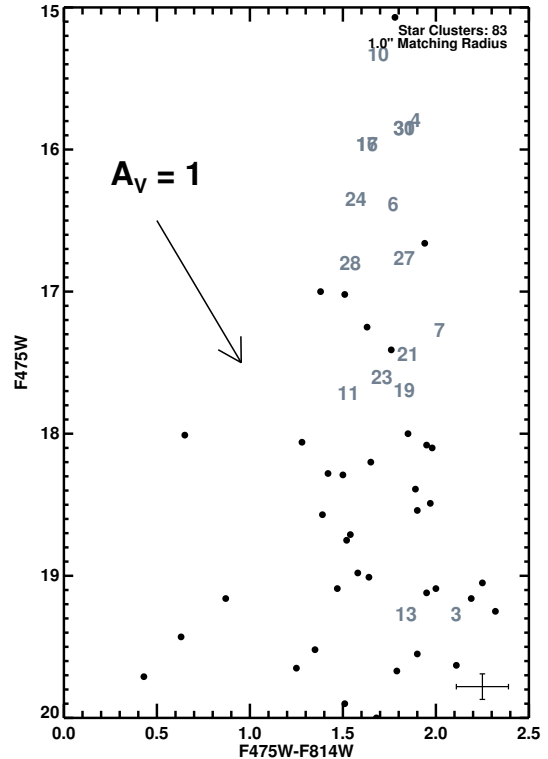


Figure 5. Color-magnitude diagram of the 83 star clusters from the catalogue of J12 in the field of view of the *Chandra* data in M31. Numbers labelling individual data points indicate the AE IDs of the 17 unique X-ray point sources that matched to 15 star clusters (Table 4). The foreground reddening vector is of length $A_V = 1$ mag. Most of the matched star clusters are brighter and redder than the remaining sample, as expected for clusters that host X-ray sources.

4. X-RAY STACKING

To study the faint population of X-ray sources we performed a stacking analysis of the 68 unmatched star clusters and 1556 unmatched H II regions in M31. Using the techniques of Brandt et al. (2001b,c) and Hornschemeier et al. (2001) we stacked 31 by 31 (45 by 45) pixel regions centered on star cluster (H II region) positions in X-ray images of M31.

Star cluster (H II region) positions closer than 16 (23) pixels to the edge of an X-ray image were excluded since each image in the stack has to be complete (i.e. cannot have null data in any pixels). This left a total of 54 star clusters and 1386 H II regions in each sample. Since there are only a handful of star clusters and they are all older than 1 Gyr we do not subdivide the population by color. However, because brighter and smaller clusters preferentially host X-ray sources we do filter¹² by R_{eff} and F475W magnitude (see Table 9) to take ad-

¹¹ Uncertainties were not published for radii and H α luminosities so we computed the standard error of the mean.

¹² We chose our filter cutoffs based on the histograms for radius and magnitude.

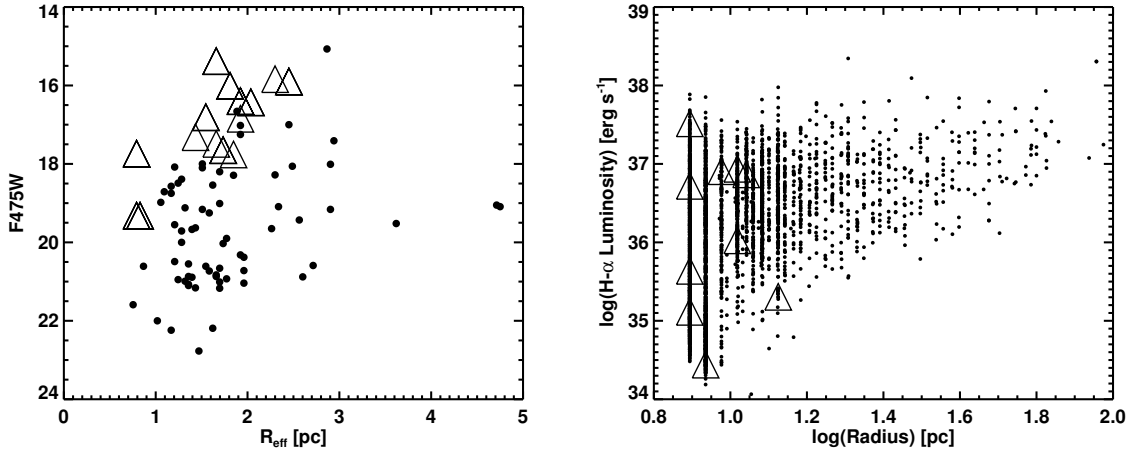


Figure 6. F475W magnitude vs. effective radius R_{eff} for the 83 star clusters in M31 (J12) that are within the field of view of the *Chandra* data (left) and $L_{\text{H}\alpha}$ vs. radius for the 1566 H II regions in the field of view of the *Chandra* data (right). Triangles indicate the matches to X-ray point sources from Tables 4 and 6. X-ray sources are preferentially found in luminous, compact star clusters. The apparent preference for compact H II regions to host X-ray sources is an artifact of their distribution (much larger number of compact H II regions). A statistical analysis (see Section 3.3) showed that neither the radius nor $\text{H}\alpha$ luminosity was a predictor of whether an H II region would host an X-ray source.

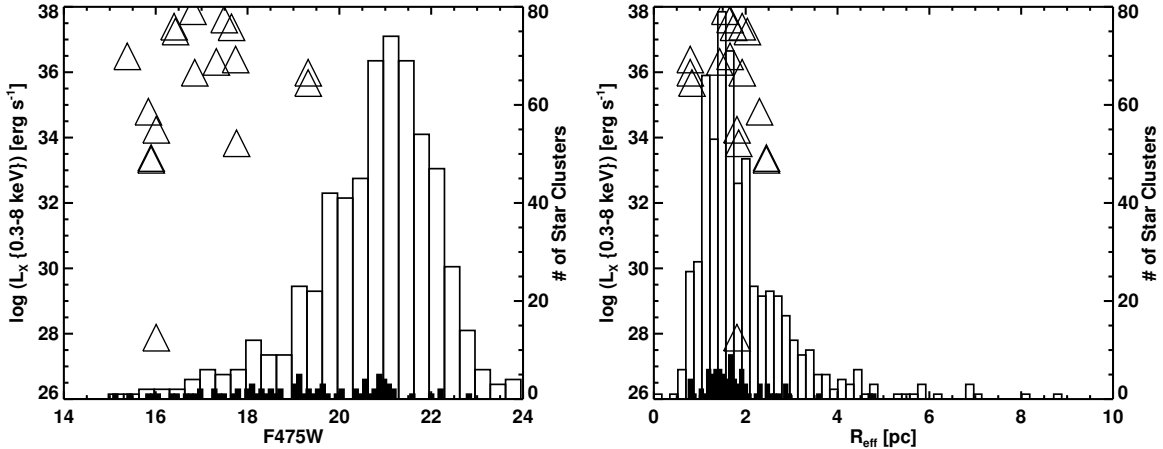


Figure 7. The X-ray luminosity of star cluster matches compared with the F475W magnitude (left) and effective radius R_{eff} (right) of star clusters. The X-ray luminosity is that of the X-ray point source matched to the star cluster and was determined by ACIS Extract (see Section 2.1.2). The 83 star clusters in the field of view of the *Chandra* data are shown in the filled black histogram while the entire year 1 PHAT survey star cluster sample is represented by the larger unfilled histogram. Triangles indicate the matches to X-ray point sources from Tables 4 and 6. Our sample has preferentially more bright clusters than the complete year 1 sample while the distributions of effective radius in the two samples appear consistent. A KS test confirmed these conclusions (see Section 3.3).

vantage of these trends. We followed a similar method for H II regions. There are two peaks in the luminosity function for H II regions in M31, at 10^{35} erg s^{-1} and 4×10^{36} erg s^{-1} for B stars and O stars respectively (Azimlu et al. 2011). These values were used to separate the population by luminosity when stacking. We stacked star clusters and H II regions in the full (0.3 – 8 keV), hard (2 – 8 keV), and soft (0.3 – 2 keV) energy bands. Sample stacked images of star clusters and H II regions are shown in Figure 8.

The net counts in the source aperture $C_n = C_s - C_b \times A_s/A_b$, where C and A represent the counts and area respectively for the source (s) and background (b) regions. The source region for star clusters in a stacked image is $1''$ (2 pixels) in radius, which corresponds to the radius used to match star clusters to X-ray point sources. Keeping the source aperture radius consistent with the matching radius ensures that we do not include any X-ray sources outside of the original matching radius in our stacked images. The background region is de-

fined to be outside the 90% encircled energy radius of the source aperture, which for star clusters that are $4'$ off-axis from the *Chandra* aimpoint is 10 pixels¹³. H II regions are more extended and also randomly distributed throughout the ACIS field of view compared to star clusters. Average off-axis angles for H II regions are not much larger than $8'$ and so we use a 20 pixel diameter for the background region (corresponding to 90% encircled energy radius for sources $8'$ off-axis). A negative source aperture luminosity results when the background-subtracted source aperture counts are <0 . This means that the background has a larger average value per pixel than the source aperture. We use Poisson statistics (method of Gehrels 1986) to calculate our uncertainties. We computed the 3σ -clipped mean μ (C_b/A_b) in the background, where pixels with counts $> \mu + 3\sigma$ were excluded. Upper and lower

¹³ Most star clusters are found in the bulge and thus are within $\sim 4'$ of the aimpoint for ACIS observations (centered on the supermassive black hole).

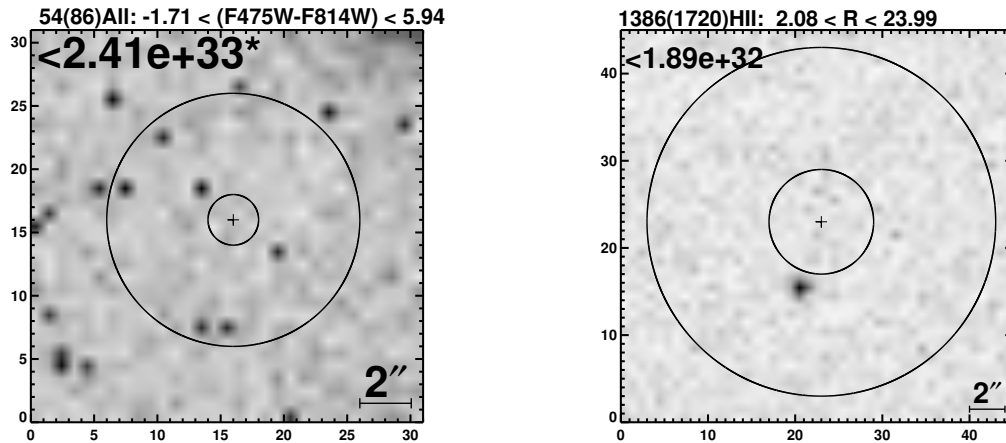


Figure 8. Stacked *Chandra* images (0.3 – 8 keV) of all 54 unique star clusters (left) and 1386 unique H II regions (right) in M31 (total number from ACIS-I and ACIS-S in brackets). Star cluster color range (H II region radius in pc) is also indicated. Pixels are $0.492''$ with 31 (45) per side. North is up and east is to the left. The source aperture is 4 (12) pixels in diameter while the background was calculated outside the larger aperture of diameter 10 (20) pixels. The value in the top left corner indicates the 1.3σ upper limit per star cluster (H II region) in the stack on the source luminosity in erg s^{-1} (asterisk denotes a negative luminosity in the source aperture). The grayscale represents the brightest pixel (darkest) relative to the dimmest pixel (lightest). All stacked images of star clusters and H II regions across all energy bands resulted in non-detections.

limits for both the source and background regions were calculated using equations (9) and (14) from Gehrels (1986), using $S = 1.282$ (number of Gaussian σ) and confidence level parameters $\beta = 0.01$ and $\gamma = -4.0$. Uncertainties in the net counts C_n were calculated by normalizing background values to those of the source aperture. Luminosities for stacked images were computed from fluxes¹⁴ ($\text{photons cm}^{-2} \text{s}^{-1}$) using a power-law spectrum with $\Gamma=1.7$ for each energy band and assuming a distance of 776 kpc. Uncertainties for luminosities were determined by multiplying the ratio of luminosity to counts in the source aperture by the uncertainties in counts. We use a larger size for our stacked images of H II regions (45 pixels) than star clusters (31 pixels) since H II regions have larger average radii. A caveat to our method is that our merged X-ray images of M31 have an inconsistent PSF at any point in the complete ACIS-I or ACIS-S image. This is a result of observations overlapping at different off-axis angles. This compounds the problem of stacking since we already introduce the same type of effect by stacking objects at various off-axis angles. All stacking completed on star clusters and H II regions resulted in non-detections. The results are displayed in Table 9 and shown graphically in Figure 9. Correcting for foreground absorption (assuming a Galactic N_{H} value of $6.6 \times 10^{20} \text{ cm}^{-2}$ (Dickey & Lockman 1990) and a power-law spectrum of $\Gamma \sim 1.7$) would increase all our luminosities by $\sim 14\%$.

5. DISCUSSION

5.1. Star Clusters

Since we analyzed the bulge of M31, which is comprised of an old stellar population and thus globular clusters, it is not surprising that our X-ray point sources are predominantly GC-LMXBs (Table 4). When comparing the averages of star cluster colour, magnitude, and effective radius our results showed that redder, brighter, and compact star clusters were more likely to host X-ray sources. However, a logistic regression analysis showed that the F475W magnitude is the most significant predictor followed by the effective radius.

The F475W–F814W color (an indicator of metallicity in old stellar populations) was not a significant predictor of whether a cluster hosted an X-ray source. A statistical analysis using logistic regression is a more robust method than comparing averages and as such accurately represents trends in the data. Peacock et al. (2010b) found different trends when using *XMM-Newton* observations of M31 to identify 45 GC-LMXBs, namely that the stellar collision rate (proportional to stellar density and core radius), luminosity, and metallicity are all significant. However, Agar & Barmby (2013) came to similar conclusions to ours when using *HST* data to derive structural parameters for 29 GC-LMXBs, and complementing the sample with published values for a total of 41 GC-LMXBs and 65 non-LMXB GCs. They found the probability of a GC hosting an X-ray source increased with increasing collision rate and proximity to the galaxy center. Metallicity was not as important a predictor but an increasing cluster mass at fixed collision rate decreased the probability of hosting an X-ray source (although the authors stress this may be a sample selection effect). The latter result does not agree with our positive trend between GC magnitude (which scales with mass) and a GC’s probability of hosting an LMXB. This discrepancy could be due to our limited sample of bulge GCs that do not have as wide a range in metallicity as GCs at larger galactocentric distances.

Studies of the GC-LMXB connection in spiral galaxies are limited. Rangelov et al. (2012) studied XRBs in the Antennae galaxies and found that massive young star clusters are more likely to host an X-ray source than less massive young clusters. When studying 32 GC-LMXBs in the spiral galaxy M104 with *Chandra*, Di Stefano et al. (2003) found that metal-rich GCs were more likely to host an X-ray source. Bellazzini et al. (1995) found similar trends in the Milky Way. Peacock et al. (2010b) does mention that the observed trends in M31 are weaker than those found for elliptical galaxies, which further stresses the need to analyze the updated star cluster data from PHAT with *Chandra*, along with surveys of other spiral galaxies.

Our stacking results gave upper limits of $\approx 10^{32} \text{ erg s}^{-1}$ across all bands for different stacks. When stacking star clus-

¹⁴ See section 2.1.1 for details on exposure-corrected images.

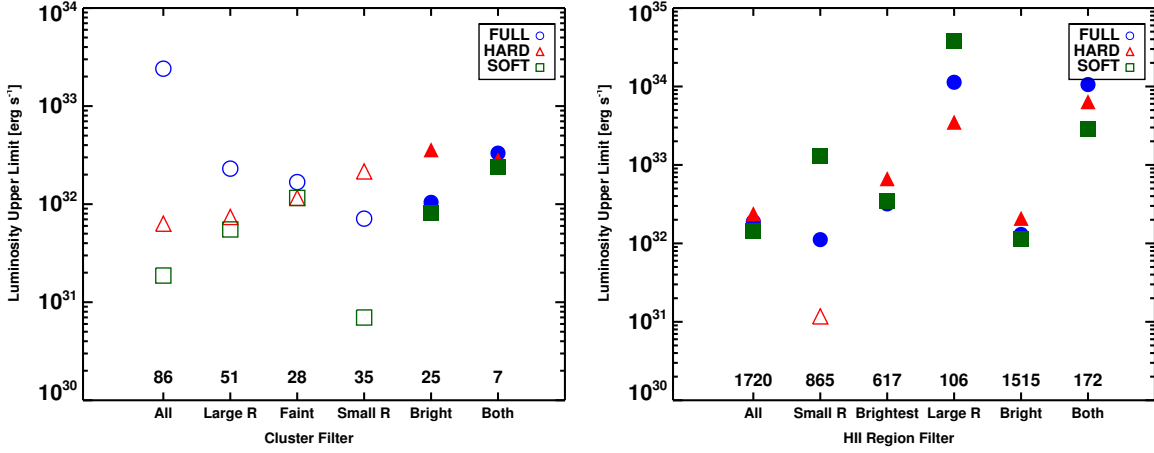


Figure 9. Upper limits in erg s^{-1} for a specific filter type in the full band (circles), hard band (triangles), and soft band (squares) for star clusters (left) and H II regions (right). Values above the x-axis indicate the total number of stacked objects (see Table 9 for the filter ranges). Filled shapes represent positive source luminosities while empty shapes are negative source luminosities (background-subtracted source aperture counts < 0). When stacking star clusters with the ‘bright’ and ‘both’ (bright and small) filters we see that the source aperture luminosity becomes positive (average pixel value is larger than the background). This can be attributed to the higher probability of brighter and (in combination) more compact clusters hosting X-ray sources. Star cluster upper limits are approximately two orders of magnitude fainter than those found for M51 (Vulic et al. 2013).

ters that were brightest (F475W magnitude), most compact (smallest R_{eff}), and a combination of the two, we found that the detection significance¹⁵ increased across all bands, although not to a statistically significant level. Due to the proximity of M31 the upper limits are approximately two orders of magnitude smaller than for star clusters in M51 (Vulic et al. 2013). Studies of globular clusters in the Milky Way have found a plethora of faint X-ray sources that include quiescent XRBs (typically $L_X \sim 10^{33} \text{ erg s}^{-1}$) (Heinke et al. 2005, 2006, 2009, 2010; Bahramian et al. 2014). In GC 47 Tucanae, five classified quiescent LMXBs had a mean $L_X(0.5 - 2.5 \text{ keV}) \approx 10^{32} \text{ erg s}^{-1}$ (Heinke et al. 2005). Therefore, assuming M31’s GCs are similar to those in the Milky Way, we should be probing this population with our stacking analysis. Given that a single GC may only have a handful of faint LMXBs, even our stacked sample of 4 of the brightest and smallest GCs fails to provide a detection. At this point it seems that stacking star clusters to identify faint XRBs is proving difficult, at least in spiral galaxies/crowded fields. With the higher concentration of X-ray sources in galaxy bulges source crowding is a problem. Along with diffuse emission in spiral disks, this complicates stacking analyses. Specifically, the background level of each image in a stack is larger making it more difficult to detect faint sources in the aperture. Ultimately a detailed, deep survey of a large sample of GCs in an early-type galaxy would be most promising for obtaining a stacking detection.

5.2. H II Regions

H II regions emit thermal X-rays at $kT \sim 0.2 - 0.3$ and $0.6 - 0.7 \text{ keV}$ due to shocks from OB star winds and supernovae/supernova remnants (Strickland et al. 2000; Grimes et al. 2005; Tüllmann et al. 2009; Mineo et al. 2012b; Li & Wang 2013). The lifetimes of H II regions (a few Myr) are long enough that HMXBs can form, providing another possible source of X-ray emission. Therefore we would expect X-ray emission in H II regions to come from various sources, with bright HMXBs and supernova remnants (if present) dominating. Tüllmann et al. (2009) found an HMXB

in the giant H II region IC131 in M33, while Ducci et al. (2013) found 2 HMXB candidates in H II regions in M83. Berghea et al. (2013) studied ultraluminous X-ray sources in nearby galaxies and concluded that 18 of 27 were located inside OB associations or star forming regions. However, most HMXBs are not found in H II regions or OB associations. In the Milky Way, Bodaghee et al. (2012) found clustering between 79 HMXBs and 458 OB associations (7σ for distances $< 1 \text{ kpc}$). The average offset of $0.4 \pm 0.2 \text{ kpc}$ between HMXBs and OB associations was consistent with compact object natal kicks of $100 \pm 50 \text{ km s}^{-1}$. The average kinematical age (time from supernova to HMXB phase) was $\sim 4 \text{ Myr}$. A follow up to this work by Coleiro & Chaty (2013) found the upper limit on kinematical age to be $\sim 3 \text{ Myr}$. Therefore unless natal kicks are small HMXBs could be located $\approx 6.5'$ (400 pc) from H II regions in M31. Based on these results one would expect most X-ray emission from H II regions to be thermal rather than from XRBs.

From Table 6 most of the previous classifications for H II regions hosting X-ray point sources in M31 have been supernova remnants as opposed to HMXBs. However, these are only supernova remnant candidates that have been found using optical line ratios ($\text{H}\alpha/\text{S II}$). In addition, our X-ray color-color plot (Figure 3) shows that none of the X-ray point sources appear in the supernova remnant regime. When comparing the average radii of matched and unmatched H II regions those that were more compact were the most likely hosts of X-ray sources. Nevertheless, a logistic regression analysis showed that both the luminosity and radius of an H II region were not significant predictors of it hosting an X-ray source. The four H II region matches that are previously unidentified can be classified as HMXB candidates and require further analysis to determine their nature. As with star clusters our stacking results of H II regions gave upper limits of $\approx 10^{32} \text{ erg s}^{-1}$ across all bands for most stacks. We saw the most improvement in detection significance (soft band) when filtering by the smallest radii ($< 8.5 \text{ pc}$) and $L_{\text{H}\alpha} > 4 \times 10^{36} \text{ erg s}^{-1}$, although not to a statistically significant level.

5.3. Chandra Coverage of M31

¹⁵ aperture luminosity / aperture upper limit

While most of the *Chandra* observations have been restricted to the central region of M31, an extension of the data to the disk is necessary to probe both young star clusters and the numerous H II regions. The resolution of X-ray data that does cover most of M31 (i.e. *XMM-Newton* and *ROSAT*) is not sufficient to distinguish individual X-ray point sources in crowded regions or reliably associate them with clusters. More specifically, with the exquisite resolution of *HST* observations such as the PHAT survey only *Chandra* will allow for robust identification of X-ray counterparts.

Figure 1 is truly striking. While *Chandra* ACIS-I data does cover a large portion of the first 8 bricks of the PHAT survey, the remaining bricks and almost the entire northeast quadrant of M31 are unobserved. In M31, *Chandra* has been used mostly for a long-term monitoring program of the supermassive black hole in the nucleus. Other observations throughout the galaxy were used to study supersoft X-ray sources. Due to the degradation of the PSF at large off-axis angles, data outside of the ACIS-S3 chip has poor resolution and therefore is not useful even for stacking. Further motivation lies in the absence of a confirmed HMXB in M31, which can be addressed by using both the H II region and star cluster catalogues available to identify candidates. Investigating the spiral arm regions that the PHAT survey has observed with (future) complementary *Chandra* data would be invaluable to furthering our understanding of the XRB population in M31.

6. SUMMARY

We used all 121 publicly available *Chandra* ACIS observations of M31 to complete a study of star clusters and H II regions. Specifically, we analyzed 83 star clusters in the bulge of M31 from the PHAT survey and found 15 unique matches (18%) to 17 X-ray point sources within 1'' (3.8 pc). When correcting our percentage of matches to completeness limits of past surveys we found similar results. The most compact, brightest, and reddest clusters preferentially hosted X-ray sources, on average. Logistic regression showed that the star cluster F475W magnitude was the most important predictor of finding a star cluster X-ray source. This follows from the fact that the most luminous and therefore most massive star clusters are more likely to host XRBs. A less significant predictor was R_{eff} , which associated smaller star clusters (probes compactness to some extent) with X-ray sources. The link between these two properties and XRBs stems from the high densities and larger number of stars that create dynamical conditions most favorable for the formation of XRBs. The F475W–F814W color, an indicator of metallicity in old stellar populations, was not a significant predictor for star clusters hosting X-ray point sources. The majority of clusters in our sample are metal-rich and thus we do not have an evenly distributed sample of blue and red clusters. A more complete survey with a larger spread in metallicity is required to confirm this result. A stacking analysis resulted in non-detections across all energy bands and average upper limits of $\approx 10^{32}$ erg s⁻¹. This is consistent with quiescent XRB luminosities in the Milky Way.

From 1566 H II regions in the field of view of the *Chandra* data only 10 matched to 9 unique X-ray point sources within 3'' (11 pc). On average, the matches corresponded to the most compact H II regions. However, a logistic regression analysis showed that neither the radius nor $H\alpha$ luminosity was a significant predictor of an H II region hosting an X-ray source. From previous optical emission-line classifications most of these sources were supernova remnant candidates.

Four sources that have no previous optical identifications are HMXB candidates. A stacking analysis resulted in upper limits of $\approx 10^{32}$ erg s⁻¹ for all energy bands. To advance our understanding of the XRB population in M31, specifically the disk, and probe the faintest extragalactic XRBs, a complete *Chandra* survey of the PHAT region is necessary.

We thank the referee for detailed comments that improved the manuscript. We also thank Ben Williams for helpful comments and Cliff Johnson for the PHAT footprint. Support for this work was provided by Discovery Grants from the Natural Sciences and Engineering Research Council of Canada and by Ontario Early Researcher Awards. We have also used the Canadian Advanced Network for Astronomical Research (CANFAR; Gaudet et al. 2011). This research has made use of the NASA/IPAC Extragalactic Database (NED), which is operated by the Jet Propulsion Laboratory, California Institute of Technology, under contract with the National Aeronautics and Space Administration. We acknowledge the following archives: the Hubble Legacy Archive (hla.stsci.edu), Chandra Data Archive (cda.harvard.edu/chaser), and 2MASS (ipac.caltech.edu/2mass).

Facilities: HST (ACS, WFC3), CXO (ACIS)

REFERENCES

Agar, J. R. R. & Barmby, P. 2013, *AJ*, 146, 135
 Antoniou, V., Zezas, A., Hatzidimitriou, D., & McDowell, J. C. 2009, *ApJ*, 697, 1695
 Arnaud, K. A. 1996, in *Astronomical Data Analysis Software and Systems V*, ed. G. H. Jacoby & J. Barnes, Vol. 101 (ASP Conference Series), 17
 Azimlu, M., Marciniak, R., & Barmby, P. 2011, *AJ*, 142, 139
 Bahramian, A., Heinke, C. O., Sivakoff, G. R., et al. 2014, *ApJ*, 780, 127
 Barnard, R., Galache, J. L., Garcia, M. R., et al. 2012a, *ApJ*, 756, 32
 Barnard, R., Garcia, M., & Murray, S. S. 2012b, *ApJ*, 757, 40
 Barnard, R., Garcia, M. R., & Murray, S. S. 2013, *ApJ*, 770, 148
 Barnard, R., Garcia, M. R., Primini, F., et al. 2014, *ApJ*, 780, 83
 Belczynski, K., Kalogera, V., Rasio, F. A., et al. 2008, *ApJS*, 174, 223
 Bellazzini, M., Pasquali, A., Federici, L., Ferraro, F. R., & Pecci, F. F. 1995, *ApJ*, 439, 687
 Bergeha, C. T., Dudik, R. P., Tincher, J., & Winter, L. M. 2013, *ApJ*, 776, 100
 Bhadkamkar, H. & Ghosh, P. 2012, *ApJ*, 746, 22
 Bhadkamkar, H. & Ghosh, P. 2013, *ArXiv e-prints*
 Bhadkamkar, H. & Ghosh, P. 2014, *ApJ*, 784, 97
 Bodaghee, A., Tomsick, J. A., Rodriguez, J., & James, J. B. 2012, *ApJ*, 744, 108
 Bondi, H. & Hoyle, F. 1944, *MNRAS*, 104, 273
 Brandt, W. N., Alexander, D. M., Hornschemeier, A. E., et al. 2001a, *AJ*, 122, 2810
 Brandt, W. N., Hornschemeier, A. E., Alexander, D. M., et al. 2001b, *AJ*, 122, 1
 Brandt, W. N., Hornschemeier, A. E., Schneider, D. P., et al. 2001c, *ApJ*, 558, L5
 Broos, P. S., Townsley, L. K., Feigelson, E. D., et al. 2010, *ApJ*, 714, 1582
 Caldwell, N., Schiavon, R., Morrison, H., Rose, J. A., & Harding, P. 2011, *AJ*, 141, 61
 Clark, G. W. 1975, *ApJ*, 199, L143
 Coleiro, A. & Chaty, S. 2013, *ApJ*, 764, 185
 Dalcanton, J. J., Williams, B. F., Lang, D., et al. 2012, *ApJS*, 200, 18
 Di Stefano, R., Kong, A. K. H., VanDalsen, M. L., et al. 2003, *ApJ*, 599, 1067
 Dickey, J. M. & Lockman, F. J. 1990, *ARA&A*, 28, 215
 Ducci, L., Sasaki, M., Haberl, F., & Pietsch, W. 2013, *A&A*, 553, A7
 Fabbiano, G. 2006, *ARA&A*, 44, 323
 Fabian, A. C., Pringle, J. E., & Rees, M. J. 1975, *MNRAS*, 172, 15P
 Fruscione, A., McDowell, J. C., Allen, G. E., et al. 2006, in *Society of Photo-Optical Instrumentation Engineers (SPIE) Conference Series*, Vol. 6270, CIAO: Chandra's data analysis system

- Gaudet, S., Armstrong, P., Ball, N., et al. 2011, in *Astronomical Society of the Pacific Conference Series*, Vol. 442, *Astronomical Data Analysis Software and Systems XX*, ed. I. N. Evans, A. Accomazzi, D. J. Mink, & A. H. Rots, 61
- Gehrels, N. 1986, *ApJ*, 303, 336
- Gilfanov, M. 2004, *MNRAS*, 349, 146
- Gordon, K. D., Bailin, J., Engelbracht, C. W., et al. 2006, *ApJ*, 638, L87
- Graessle, D. E., Evans, I. N., Glotfelty, K., et al. 2006, in *Society of Photo-Optical Instrumentation Engineers (SPIE) Conference Series*, Vol. 6270, *The Chandra X-ray Observatory calibration database (CalDB): building, planning, and improving*
- Grimes, J. P., Heckman, T., Strickland, D., & Ptak, A. 2005, *ApJ*, 628, 187
- Grimm, H.-J., Gilfanov, M., & Sunyaev, R. 2002, *A&A*, 391, 923
- Grimm, H.-J., Gilfanov, M., & Sunyaev, R. 2003, *MNRAS*, 339, 793
- Heinke, C. O., Altamirano, D., Cohn, H. N., et al. 2010, *ApJ*, 714, 894
- Heinke, C. O., Cohn, H. N., & Lugger, P. M. 2009, *ApJ*, 692, 584
- Heinke, C. O., Grindlay, J. E., Edmonds, P. D., et al. 2005, *ApJ*, 625, 796
- Heinke, C. O., Grindlay, J. E., Lugger, P. M., et al. 2003, *ApJ*, 598, 501
- Heinke, C. O., Wijnands, R., Cohn, H. N., et al. 2006, *ApJ*, 651, 1098
- Hofmann, F., Pietsch, W., Henze, M., et al. 2013, *A&A*, 555, A65
- Hornschemeier, A. E., Brandt, W. N., Garmire, G. P., et al. 2001, *ApJ*, 554, 742
- Hurley, J. R., Tout, C. A., & Pols, O. R. 2002, *MNRAS*, 329, 897
- Iben, Jr., I., Tutukov, A. V., & Yungelson, L. R. 1995, *ApJS*, 100, 217
- Johnson, L. C., Seth, A. C., Dalcanton, J. J., et al. 2012, *ApJ*, 752, 95
- Kaaret, P. 2002, *ApJ*, 578, 114
- Katz, J. I. 1975, *Nature*, 253, 698
- Kiel, P. D. & Hurley, J. R. 2006, *MNRAS*, 369, 1152
- Kilgard, R. E., Cowan, J. J., Garcia, M. R., et al. 2005, *ApJS*, 159, 214
- Kim, D.-W. & Fabbiano, G. 2004, *ApJ*, 611, 846
- Kim, D.-W., Fabbiano, G., Ivanova, N., et al. 2013, *ApJ*, 764, 98
- Kong, A. K. H., Garcia, M. R., Primini, F. A., et al. 2002, *ApJ*, 577, 738
- Lehmer, B. D., Alexander, D. M., Bauer, F. E., et al. 2010, *ApJ*, 724, 559
- Li, J.-T. & Wang, Q. D. 2013, *MNRAS*, 428, 2085
- Lipunov, V. M., Postnov, K. A., Prokhorov, M. E., & Bogomazov, A. I. 2009, *Astronomy Reports*, 53, 915
- Lutovinov, A. A., Revnitvsev, M. G., Tsygankov, S. S., & Krivonos, R. A. 2013, *MNRAS*, 431, 327
- Marigo, P., Girardi, L., Bressan, A., et al. 2008, *A&A*, 482, 883
- Massey, P., Olsen, K. A. G., Hodge, P. W., et al. 2006, *AJ*, 131, 2478
- Mineo, S., Fabbiano, G., D'Abrusco, R., et al. 2014, *ApJ*, 780, 132
- Mineo, S., Gilfanov, M., & Sunyaev, R. 2012a, *MNRAS*, 419, 2095
- Mineo, S., Gilfanov, M., & Sunyaev, R. 2012b, *MNRAS*, 426, 1870
- Muno, M. P., Bauer, F. E., Baganoff, F. K., et al. 2009, *ApJS*, 181, 110
- Nebot Gómez-Morán, A., Motch, C., Barcons, X., et al. 2013, *A&A*, 553, A12
- Paolillo, M., Puzia, T. H., Goudfrooij, P., et al. 2011, *ApJ*, 736, 90
- Peacock, M. B., Maccarone, T. J., Knigge, C., et al. 2010a, *MNRAS*, 402, 803
- Peacock, M. B., Maccarone, T. J., Kundu, A., & Zepf, S. E. 2010b, *MNRAS*, 407, 2611
- Persic, M. & Rephaeli, Y. 2007, *A&A*, 463, 481
- Pooley, D., Lewin, W. H. G., Anderson, S. F., et al. 2003, *ApJ*, 591, L131
- R Development Core Team. 2008, *R: A Language and Environment for Statistical Computing*, R Foundation for Statistical Computing, Vienna, Austria, ISBN 3-900051-07-0
- Ranalli, P., Comastri, A., & Setti, G. 2003, *A&A*, 399, 39
- Rangelov, B., Chandar, R., Prestwich, A., & Whitmore, B. C. 2012, *ApJ*, 758, 99
- Revnitvsev, M., Lutovinov, A., Churazov, E., et al. 2008, *A&A*, 491, 209
- Sazonov, S., Revnitvsev, M., Gilfanov, M., Churazov, E., & Sunyaev, R. 2006, *A&A*, 450, 117
- Shaw Greening, L., Barnard, R., Kolb, U., Tonkin, C., & Osborne, J. P. 2009, *A&A*, 495, 733
- Shtykovskiy, P. E. & Gilfanov, M. R. 2007, *Astronomy Letters*, 33, 299
- Siess, L., Izzard, R. G., Davis, P. J., & Deschamps, R. 2013, *A&A*, 550, A100
- Sivakoff, G. R., Jordán, A., Sarazin, C. L., et al. 2007, *ApJ*, 660, 1246
- Skrutskie, M. F., Cutri, R. M., Stiening, R., et al. 2006, *AJ*, 131, 1163
- Stiele, H., Pietsch, W., Haberl, F., et al. 2011, *A&A*, 534, A55
- Strickland, D. K., Heckman, T. M., Weaver, K. A., & Dahlem, M. 2000, *AJ*, 120, 2965
- Swartz, D. A., Ghosh, K. K., Tennant, A. F., & Wu, K. 2004, *ApJS*, 154, 519
- Swartz, D. A., Soria, R., Tennant, A. F., & Yukita, M. 2011, *ApJ*, 741, 49
- Taylor, M. B. 2005, in *Astronomical Society of the Pacific Conference Series*, Vol. 347, *Astronomical Data Analysis Software and Systems XIV*, ed. P. Shopbell, M. Britton, & R. Ebert, 29
- Trudolyubov, S. & Priedhorsky, W. 2004, *ApJ*, 616, 821
- Tüllmann, R., Long, K. S., Pannuti, T. G., et al. 2009, *ApJ*, 707, 1361
- Ubeda, L. & et al. 2012, *Advanced Camera for Surveys Instrument Handbook for Cycle 21 v. 12.0* (Baltimore: STScI)
- Voss, R. & Gilfanov, M. 2007a, *A&A*, 468, 49
- Voss, R. & Gilfanov, M. 2007b, *MNRAS*, 380, 1685
- Vulic, N., Barmby, P., & Gallagher, S. C. 2013, *ApJ*, 763, 96
- Walton, D. J., Roberts, T. P., Mateos, S., & Heard, V. 2011, *MNRAS*, 416, 1844
- Williams, B. F., Garcia, M. R., Kong, A. K. H., et al. 2004, *ApJ*, 609, 735
- Zacharias, N., Urban, S. E., Zacharias, M. I., et al. 2004, *AJ*, 127, 3043
- Zezas, A., Fabbiano, G., Rots, A. H., & Murray, S. S. 2002, *ApJ*, 577, 710
- Zhang, Z., Gilfanov, M., Voss, R., et al. 2011, *A&A*, 533, A33

Table 9
 Stacked Image Properties

Filter	Unique Number	Total Number ^a	FULL		HARD		SOFT				
			Upper Limit ^b (10^{32} erg s ⁻¹)	Sky Sigma ^d (10^{32} erg s ⁻¹)	Upper Limit ^b (10^{32} erg s ⁻¹)	Sky Sigma ^d (10^{32} erg s ⁻¹)	Upper Limit ^b (10^{32} erg s ⁻¹)	Sky Sigma ^d (10^{32} erg s ⁻¹)			
H II regions											
None	1386	1720	1.889	2.18	2.389	1.122	0.012	1.421	0.892	0.011	
R < 17 pc	711	865	1.116	2.257	0.023	0.117	1.123	0.015	13.02	0.854	0.013
L _{HII} > 4 × 10 ³⁶ erg s ⁻¹	476	617	3.186	2.032	0.041	6.678	0.983	0.025	3.435	0.674	0.021
R > 34 pc	83	106	113.128	1.794	0.08	35.079	0.175	0.011	379.804	0.064	0.005
L _{HII} > 10 ³⁵ erg s ⁻¹	1231	1515	1.3	2.16	0.02	2.087	1.104	0.013	1.121	0.872	0.012
L _{HII} > 4 × 10 ³⁶ erg s ⁻¹ & R < 17 pc	132	172	105.83	1.442	0.061	63.978	0.131	0.007	28.521	0.04	0.003
Star Clusters											
None	54	86	24.058	4.641	0.054	0.632	1.573	0.03	0.187	3.054	0.045
R _{eff} > 0.4 pc	33	51	2.302	4.42	0.069	0.74	1.473	0.038	0.553	2.871	0.057
F475W > 20.5	21	28	1.678	3.073	0.09	1.157	1.283	0.05	1.158	1.651	0.073
R _{eff} < 0.4 pc	21	35	0.711	4.952	0.089	2.156	1.693	0.05	0.07	3.276	0.074
F475W < 19	15	25	1.044	6.528	0.113	3.587	1.685	0.055	0.818	4.723	0.097
R _{eff} < 0.4 pc & F475W < 19	4	7	3.315	7.475	0.222	2.827	1.565	0.091	2.413	5.602	0.197

Note. — A foreground absorption term (assuming Galactic $N_{\text{H}} \approx 6.6 \times 10^{20}$ cm⁻² (Dickey & Lockman 1990) and a power-law spectrum of $\Gamma \sim 1.7$) would increase all our luminosities by $\sim 14\%$.

^a From ACIS-I and ACIS-S data.

^b On source aperture (radius of 1" and 3" for star clusters and H II regions respectively) luminosity.

^c The background aperture (outside a radius of 5" and 10" for star clusters and H II regions respectively) luminosity per pixel.

^d Uncertainty in the background per pixel, determined by averaging the upper and lower limits calculated using equations (9) and (14) of Gehrels (1986).